Oxygen reduction reaction and proton exchange membrane fuel cell performance of pulse electrodeposited Pt–Ni and Pt–Ni–Mo(O) nanoparticles

Konrad Eiler [a], [*], [1], Live Mølmen [b], [c], [**], [1], Lars Fast [b], Peter Leisner [c], Jordi Sort [a], [d], Eva Pellicer [a], [***]

[a] Department de Física, Universitat Autònoma de Barcelona, 08193 Bellaterra, Spain
[b] Department of Electrification and Reliability, RISE Research Institutes of Sweden, Brinellgatan 4, 50462 Borås, Sweden
[c] Department of Materials and Manufacturing, School of Engineering, Jönköping University, Gjuterigatan 5, 55111 Jönköping, Sweden
[d] Institució Catalana de Recerca I Estudis Avançats (ICREA), Pg. Lluís Companys 23, 08010 Barcelona, Spain

ARTICLE INFO

ABSTRACT

Proton exchange membrane fuel cells (PEMFCs) are an important alternative to fossil fuels and a complement to batteries for the electrification of vehicles. However, their high cost obstructs commercialization, and the catalyst material, including its synthesis, constitutes one of the major cost components. In this work, Pt–Ni and Pt–Ni–Mo(O) nanoparticles (NPs) of varying composition have been synthesized in a single step by pulse electrodeposition onto a PEMFC's gas diffusion layer. The proposed synthesis route combines NP synthesis and their fixation onto the microporous carbon layer in a single step. Both Pt–Ni and Pt–Ni–Mo(O) catalysts exhibit extremely high mass activities at oxygen reduction reaction (ORR) with very low Pt loadings of around 4 $\mu g/cm^2$ due to the favorable distribution of NPs in contact with the proton exchange membrane. Particle sizes of 40–50 nm and 40–80 nm were obtained for Pt–Ni and Pt–Ni–Mo(O) systems, respectively. The highest ORR mass activities were found for $Pt_{67}Ni_{33}$ and $Pt_{66}Ni_{32}$–MoO_x NPs. The feasibility of a single-step electrodeposition of Pt–Ni–Mo(O) NPs was successfully demonstrated; however, the ternary NPs are of more amorphous nature in contrast to the crystalline, binary Pt–Ni particles, due to the oxidized state of Mo. Nevertheless, despite their heterogeneous nature, the ternary NPs show homogeneous behavior even on a microscopic scale.

1. Introduction

The market for proton exchange membrane fuel cells (PEMFCs) is growing as the EU has highlighted hydrogen as a key factor in the energy market in their Green Deal plan [1]. One of the ways in which hydrogen shall be used is to power heavy-duty vehicles, where large storage capacity and fast refueling are crucial. To increase the competitivity of such fuel cell electric vehicles, the production cost of fuel cells needs to be reduced. Platinum-based electrocatalysts are one of the main cost-determining components, leading to an enormous research interest in the reduction of Pt content. Among the various strategies towards this goal, the alloying of Pt is one of the most promising and advanced approaches [2].

Along with the strive for cost reduction, the durability of the electrocatalysts is a major issue to be tackled. The widely used, commercially available Pt/C catalysts show a number of disadvantages with respect to oxygen reduction reaction (ORR) performance at the cathode of the PEMFC. Apart from their poor efficiency with respect to the Pt loading, their limited durability is a major drawback for reliable long-term application and sustainability [3]. Pt itself, however, is crucial for ORR especially in acidic environments such as the PEMFC. The most active transition metals at ORR and therefore worth considering for alloying with Pt are Cu, Ni, and Co [4]. The most investigated and most promising Pt-based nanoparticles (NPs) tackling durability issues are Pt–Co and Pt–Ni NPs, often in the form of core-shell NPs with a Pt shell [5,6]. Further

---

* Corresponding author.
** Corresponding author.
*** Corresponding author.
E-mail addresses: konrad.eiler@uab.cat (K. Eiler), live.molmen@ri.se (L. Mølmen), eva.pellicer@uab.cat (E. Pellicer).
[1] These authors contributed equally to this work.

effort to simultaneously improve both ORR activity and durability are sought by investigation of ternary and quaternary systems [7,8]. Apart from the composition of the electrocatalyst, a high number of active sites is targeted to achieve high catalytic efficiency [9]. For this reason, the incorporation of NPs and even single-metal atom catalysts in carbonaceous matrices is currently a subject of intense investigation [10,11].

One of the challenges, and an important factor influencing the fuel cell performance, is the synthesis route of the catalyst, which also adds up to the production cost. In most approaches, the catalyst NPs are synthesized on a carbon support, mixed with a binder and ionomer, and sprayed onto the membrane, which leads to NPs being deposited in locations where they are not accessible for the catalytic reactions [12]. Using direct electrodeposition of Pt alloy NPs onto the gas diffusion layer (GDL) of the PEMFC, the NPs are deposited on the most active sites of the carbon support because the metal ions should occupy the locations where the local electric field is highest during the electrodeposition—locations on the substrate where the path is short and the local charge density is high. Furthermore, this approach combines both synthesis and fixation (or distribution) of NPs into a single step, leading to a cost reduction of the synthesis route [13].

Fundamental research on the mechanisms of NP formation by electrodeposition has been carried out by Ustarroz et al., including the electrodeposition of Pt NPs for potential application at ORR [14–16]. The electrodeposition of Pt alloy NPs has also been shown promising for alkaline ORR and other catalytic reactions [17,18].

A common synthesis route for metallic NPs is by pulse electrodeposition. An extensive study on the pulse electrodeposition of Pt NPs for ORR was carried out by Huang et al. [19]. A pulse reverse process was employed by Sriwannaboot et al. for the codeposition of Pt–Co alloy onto carbon cloth substrates [20]. Egetenmeyer et al. thoroughly investigated the effects of pulse electrodeposition parameters for Pt, Pt–Ni, and Pt–Co NPs deposited onto GDLs, and determined optimum electrodeposition parameters for each alloy [21]. Santiago et al. were able to reduce the rather high Pt NP size commonly obtained by electrodeposition down to below 10 nm by deposition onto a rotating disk electrode (RDE) [22]. Wang et al. achieved Pt particle sizes of 3–10 nm via the use of a complexing agent [23]. Remarkably, pulse electrodeposition offers several advantages compared with other NP fabrication schemes. First, synthesis and anchoring to a substrate such as GDL is achieved in one step. Second, NPs nucleate onto the most active sites of the GDL, as aforementioned, as opposed to other post-synthesis approaches for which the catalyst is distributed on the GDL irrespective of local electrical properties and depth, so that many NPs may be located at inaccessible or unfavorable locations. The main disadvantage of pulse electrodeposition compared with conventional liquid-phase synthesis and high-temperature calcination [24] is that an increase in the catalyst loading is achieved at the expense of increasing particle size, which is often undesirable for catalytic purposes.

Interestingly, Liu et al. synthesized a Pt–Ni alloy with low Pt content via a carbothermal shock method, which was shown to be effective at ORR in acidic media and PEMFC testing [25]. This is in contrast to most ORR electrocatalysts investigated for PEMFC, which usually rely on high-Pt content alloy NPs.

Although the synthesis of Pt–Ni NPs for ORR [26,27], as well as the electrodeposition of Pt–Ni alloys in general [28,29] is well advanced, Mo-containing Pt alloys have been scarcely investigated. Huang et al. showed that the doping of Pt_3Ni NPs with Mo led to extraordinary ORR performance, making the ternary Pt–Ni–Mo system an interesting candidate for ORR studies [30]. These NPs were obtained by decomposition of acetonate and hexacarbonyl precursors. The electrochemical co-deposition of Mo, which is

usually achieved using sodium molybdate [31], may lead to the formation of intermediate Mo oxide species due to partial reduction of Mo(VI) [32]. However, even NPs containing Mo oxide show improved electrocatalytic properties [8,33]. The coordination of Mo with electronegative elements like oxygen or nitrogen can move the d-band center of Mo so that its binding capacity with reaction intermediates (O*, OH*, and OOH*) increases, thus making Mo atoms moderately active towards ORR [34]. Therefore, the introduction of oxidized Mo atoms to Pt–Ni should not be, in principle, deleterious for the ORR performance.

Considering the above results, it seems that (i) Pt–Ni is both an adequate candidate for ORR and (ii) the incorporation of a third alloying element can improve electrocatalytic performance. Yet, the expected improvement is not always attained. For example, Sorsa et al. electrodeposited Pt–Ni from liquid crystalline solution onto GDL substrates, but they did not observe any significant improvement of the electrodeposited Pt–Ni over commercial Pt/C [35]. Hence, further investigation on this topic is still to be performed.

In this work, pulse electrodeposition is used to deposit Pt–Ni and Pt–Ni–Mo(O) particles directly onto the microporous layer of a commercial GDL. The GDL is composed of a woven carbon cloth with a microporous, PTFE-coated carbon layer, where the catalysts shall be applied. For such a complex three-dimensional substrate, electrodeposition is an especially suitable method [36]. In the deposition process, all particles are deposited on the most active sites of the carbon support's surface where they guarantee excellent contact with both the support and the proton exchange membrane (PEM) in the fuel cell. Although the use of Pt–Ni NPs for ORR, and the electrodeposition of Pt–Ni alloys are rather developed, the combination of both, in addition to the direct deposition onto the GDL, has been reported very scarcely. The Pt–Ni and Pt–Ni–Mo(O) NPs with different compositions are chemically and structurally characterized, and ORR in acidic media is investigated. Finally, fuel cell performance and durability tests in a PEMFC prototype are carried out after hot-pressing the obtained cathodes with the PEM and a commercial Pt/C electrode as anode.
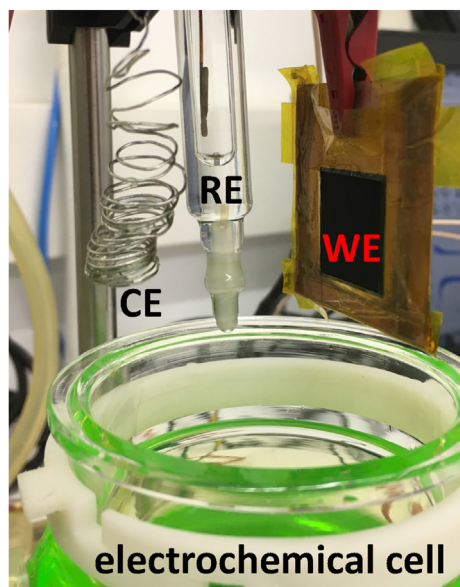
2. Experimental

2.1. NP synthesis

The synthesis of Pt–Ni and Pt–Ni–Mo(O) NPs was performed by pulse electrodeposition from aqueous solution in a three-electrode electrochemical cell. An Autolab PGSTAT204 potentiostat/galvanostat was used with a Pt wire as counter electrode (CE), an Ag|AgCl (3 M KCl) reference electrode (RE) and a working electrode (WE). The WE consisted of a 2 cm by 2 cm GDL, supplied by Freudenberg, mounted on a Cu support to ensure electrical connection and a homogeneous charge distribution over the entire area of the GDL during electrodeposition. The excessive area of the Cu support was isolated with polyimide tape (Fig. 1).

The aqueous electrolytes were loaded with nickel chloride, sodium hexachloroplatinate, boric acid, and ammonium chloride, based on an earlier study [28]. For the deposition of Pt–Ni–Mo(O), sodium molybdate (as Mo precursor) as well as citric acid as complexing agent were added (Table 1). All chemicals for electrolyte preparation were of analytical grade and had been supplied by Merck. The pH was adjusted to 2.7 by addition of sulfuric acid solution.

The electrodeposition was carried out in stagnant conditions at 30 °C with pulses of varying current density to obtain different compositions. The choice of pulse deposition parameters was initially orientated on the study on the electrodeposition of Pt–Ni NPs carried out by Egetenmeyer et al. [21] and then altered by empirically optimizing pulse deposition parameters with respect to

Fig. 1. Set-up of the three-electrode electrochemical cell with the Pt counter electrode (CE), Ag|AgCl reference electrode (RE), and the GDL mounted on a Cu plate at the working electrode (WE).

Table 1
Electrolyte composition for the deposition of Pt−Ni and Pt−Ni−Mo(O) nanoparticles.

	Pt−Ni	Pt−Ni−Mo(O)
200 mM	$NiCl_2$	$NiCl_2$
5 mM	$Na_2PtCl_6 \cdot 6H_2O$	$Na_2PtCl_6 \cdot 6H_2O$
200 mM	H_3BO_3	H_3BO_3
25 mM	NH_4Cl	NH_4Cl
50 mM		$Na_2MoO_4 \cdot 2H_2O$
100 mM		citric acid

particle size, catalyst loading, and composition. It was observed that lower particle sizes were obtained at the expense of the catalyst loading, so that finally the process parameters were chosen as a compromise between particle size and catalyst loading. Pulse on-time and off-time were kept constant at 5 ms and 70 ms, respectively, whereas the number of cycles was changed with the current density to obtain identical deposited charges and, assuming similar Faradaic current efficiencies for each electrolyte, similar catalyst loading (Table 2). The total charge was increased for the Pt−Ni−Mo(O) deposition due to the addition of citric acid, which was observed to compromise the current efficiency. This is in accordance with previous studies, where the addition of citrate was found to increase Mo content in the deposits while lowering the current efficiency [37]. It was also observed during initial studies

Table 2
Conditions for pulse electrodeposition of Pt−Ni and Pt−Ni−Mo(O) NPs. For the sake of comparison, the atomic composition of the ternary NPs is given as if Mo were fully reduced.

Cathodic peak current density [mA/cm^2]	Number of cycles	Composition
31	240	$Pt_{79}Ni_{21}$
37	200	$Pt_{67}Ni_{33}$
43	170	$Pt_{80}Ni_{20}$
49	150	$Pt_{73}Ni_{27}$
54	920	$Pt_{78}Ni_{21}Mo_1$
77	640	$Pt_{66}Ni_{32}Mo_2$
100	490	$Pt_5Ni_{71}Mo_{24}$
123	440	$Pt_5Ni_{74}Mo_{21}$

that higher current densities were needed for the ternary NPs to obtain the desired particle size and composition.

2.2. Electrochemical characterization

The same three-electrode set-up used for NP electrodeposition was used for cyclic voltammetry (CV) studies of the NP/C assemblies in 0.5 M H_2SO_4 to activate the catalysts and to determine their electrochemically active surface area (ECSA). To this end, 30 cycles at 200 mV/s and 5 cycles at 50 mV/s were recorded in a potential window between 0 and 1.3 V versus reversible hydrogen electrode (RHE). ORR was studied by CV in O_2-saturated 0.1 M $HClO_4$ after recording a background CV in N_2-saturated electrolyte, both at 10 mV/s between 0 and 1.1 V versus RHE and in static conditions. Potentials applied against Ag|AgCl were converted to RHE scale. The curves were corrected for Ohmic drop (*iR*-correction) after determination of the instrumentation resistance by electrochemical impedance spectroscopy (EIS) [38]. A Pt/C GDE with a Pt loading of 0.3 mg/cm^2 was tested as a reference. It should be noted that the procedure for ORR measurements employed here differs from the usual approach using RDE since the electrocatalysts are directly deposited onto the GDL substrates and cannot be deposited directly onto an RDE. As a result, a quantitative determination of ORR parameters, such as the half-wave potential, is not feasible. Nevertheless, the measurements give qualitative information to show trends between catalysts of different compositions, in addition to the comparison with a commercial GDE.
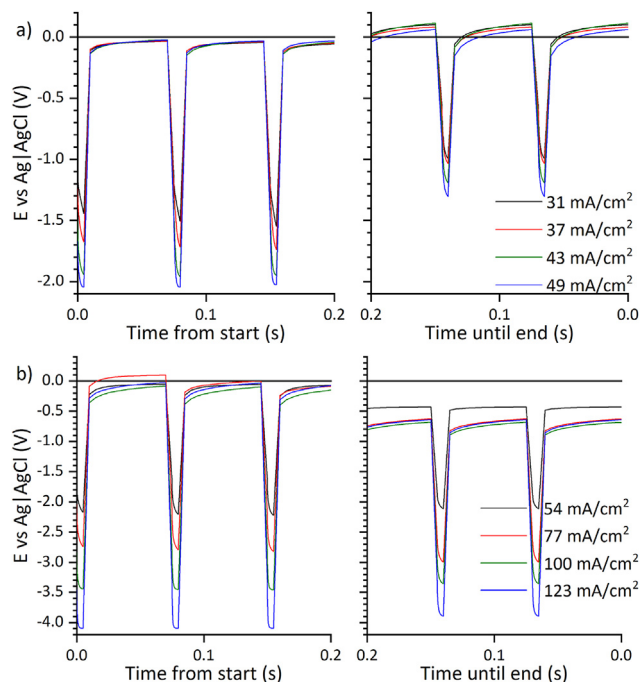
2.3. SEM

All deposited NPs, as well as the unloaded GDL substrate, were analyzed by scanning electron microscopy (SEM) on a Zeiss Merlin electron microscope to evaluate particle size, distribution, and loading of the substrates, using an acceleration voltage of 1 kV. For energy-dispersive X-ray spectroscopy (EDX), an acceleration voltage of 20 kV was used. However, quantification of the electrocatalyst NPs was not feasible by EDX due to the very low loading of NPs. For this reason, a chemical analysis method was employed (see below). Particle sizes were determined by image analysis of the SEM micrographs using ImageJ, taking the average of 100−200 particles per sample. SEM was also used for post analysis after PEMFC testing on a TESCAN LYRA3, after the cathode was delaminated from the membrane electrode assembly (MEA). For cross-sectional observation, one MEA was cut, embedded in epoxy resin, mechanically ground and polished and subsequently ion milled by Ar ions on a Gatan PECS II.

2.4. TEM

Transmission electron microscopy (TEM) was conducted on a JEOL JEM-2011 in high resolution and diffraction mode to study the crystalline structure of the NPs. Samples for TEM were prepared by scratching the catalyst NPs, together with part of the carbon support, off the electrodes, dispersing the samples in ethanol, and dropping them onto the carbon film of a TEM copper grid. Electron energy loss spectroscopy (EELS) was performed on a FEI Tecnai G^2 F20 STEM. Both TEM were working at an acceleration voltage of 200 kV.

2.5. Chemical analysis

For determination of both composition and loading of the substrates, NPs were dissolved in aqua regia, consisting of hydrochloric acid and nitric acid in a ratio of 3:1 in volume, and the concentration of Pt, Ni, and Mo in the solution was determined by inductively

Fig. 2. Initial and final pulses for pulse deposition of Pt–Ni (a) and Pt–Ni–Mo(O) (b) nanoparticles. Currents are normalized by the geometric area of the gas diffusion layer.

coupled plasma mass spectrometry (ICP-MS) on an Agilent 7500ce spectrometer for each variation of electrodeposition parameters. In addition, the Faradaic current efficiency was determined by relating the total charge converted during electrodeposition to the absolute masses of Pt, Ni, and Mo and assuming that all metals had been fully reduced from their initial oxidation state.

2.6. X-ray photoelectron spectroscopy

X-ray photoelectron spectroscopy (XPS) was performed on a PHI 5500 spectrometer to study the surface state of the NPs, recording the core spectra for C1s, Ni2p, Pt4f, and Mo2p, before and after Ar ion sputtering for 30 s, as well as on the disassembled MEAs after PEMFC testing. Peak fitting of the spectra was done by the software XPSPEAK. Energy calibration was done by positioning the main C1s peak at 284.5 eV.

2.7. Fuel cell testing

For the PEMFC testing, the cathodes containing the electro-deposited Pt–Ni and Pt–Ni–Mo(O) NPs were hot-pressed together with a Nafion 212 membrane (Chemours) and a commercial GDE

with a Pt loading of 0.3 mg/cm^2 as anode using a pressure of 0.5 MPa at 110 °C for 3 min to form the MEA.

All MEAs were tested in a single-cell fuel cell tester using coated stainless steel flow plates. The active area of the fuel cell was 2.9 cm^2. A Greenlight G20 test station was used for PEMFC tests, with a temperature of 80 °C for both gases and a dewpoint temperature of 65 °C. The flow of H$_2$ and air were 0.042 and 0.10 l$_n$/min (normal liter per minute), respectively.

The cells were activated by cycling between 0.9 V and 0.6 V for 2 000 cycles before a polarization curve was obtained. For durability testing, an accelerated stress test (AST) consisting of 20 000 additional cycles were performed, with polarization curves obtained after 10 000 cycles and at end of test (EoT).

3. Results and discussion

3.1. Electrodeposition process

For all NPs, the amplitude of the deposition potential increases with the amplitude of the current density (Fig. 2). During pulse deposition of Pt–Ni NPs, the amplitude ranges initially between −1.4 and −2.0 V versus Ag|AgCl depending on the applied current density. This potential drops towards the end of the deposition to within −1.0 to −1.3 V. The potential established during off-time changes from just below 0 V to slightly positive potential. In turn, the potential amplitudes for the deposition of ternary Pt–Ni–Mo(O) NPs ranges from −2.0 V to −4.0 V due to the higher current densities applied. Those latter potentials do seem uncommonly high, however they are based on an empirical determination of the process parameters. They may thus be the result of a significant resistivity of the GDL substrate. The potential does not change significantly until the end of deposition, whereas the potential during off-time changes to −0.6 V towards the end, showing a trend which is inverse to the one observed for binary NPs.

3.2. Characterization of the as-deposited nanoparticles
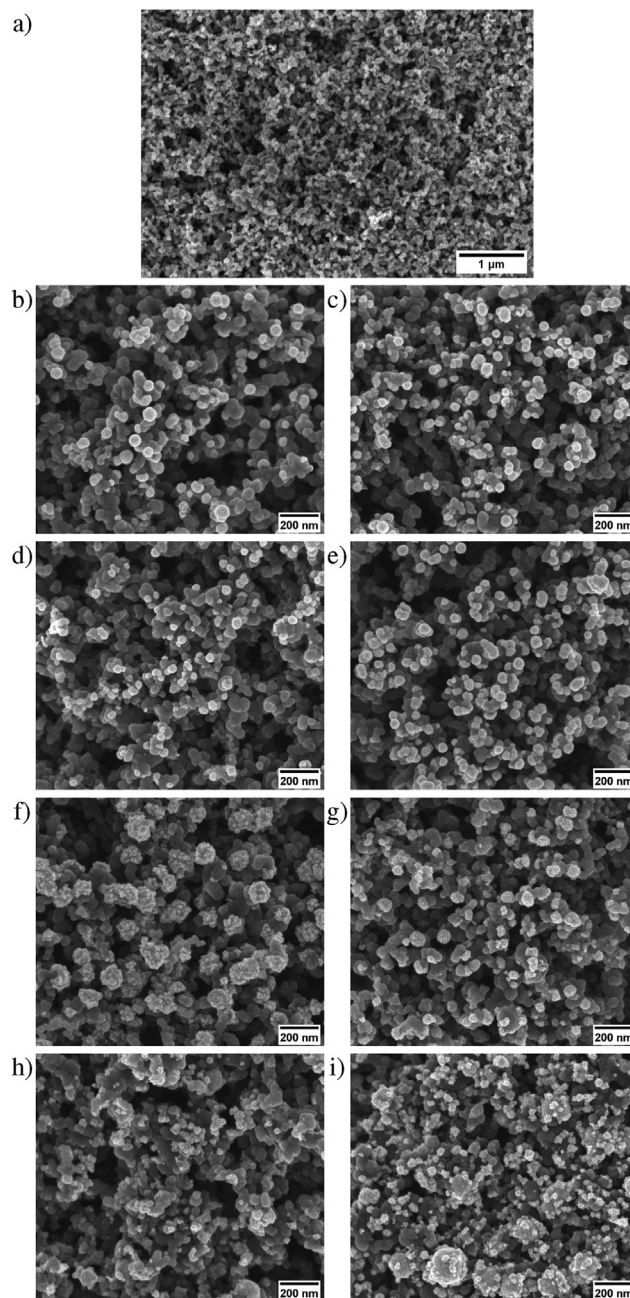
3.2.1. Chemical analysis

The results of the ICP-MS shows that all four depositions of Pt–Ni resulted in a Pt content of 67−80 at% (Table 3) and a Pt loading of 3.7−4.1 μg/cm^2. Assuming that the metal is completely reduced, which is fairly true for this case, the current efficiency is ca. 25% for all Pt–Ni depositions. However, Pt–Ni–Mo(O) appeared to pass a threshold as the current density increased from 77 to 100 mA/cm^2, where the two lower current densities resulted in similar composition to the Pt–Ni with 78 and 66 at% Pt and low amounts of 1 and 2 at% Mo, respectively. The higher current densities on the other hand resulted in very low Pt content of only 5 at% while Ni became the main constituent. The Mo content increased to 24 and 21 at%. Note that the composition of the ternary NPs is given in atomic percentage disregarding the oxygen content. The

Table 3
Summary of the determined parameters for Pt–Ni and Pt–Ni–Mo(O) nanoparticles (NPs). Current efficiency of deposition, NP size at beginning of test (BoT) and end of test (EoT), total metal catalyst and Pt loadings, electrochemically active surface area (ECSA) calculated with respect to mass of Pt, and Tafel slope b.

Composition	Current efficiency %	Mean ø BoT nm	Mean ø EoT nm	Catalyst loading μg/cm^2	Pt loading μg/cm^2	ECSA m^2/g$_{Pt}$	b mV
Pt$_{79}$Ni$_{21}$	23	50 ± 13	46 ± 19	4.0	3.7	36	66
Pt$_{67}$Ni$_{33}$	26	47 ± 12	44 ± 20	4.6	4.0	19	65
Pt$_{80}$Ni$_{20}$	25	40 ± 8	46 ± 20	4.4	4.1	40	65
Pt$_{73}$Ni$_{27}$	25	49 ± 9	38 ± 17	4.4	4.0	34	66
Pt$_{78}$Ni$_{21}$Mo$_1$	7	83 ± 30	45 ± 24	8.1	7.4	28	66
Pt$_{66}$Ni$_{32}$Mo$_2$	2	49 ± 14	26 ± 14	2.5	2.2	18	62
Pt$_5$Ni$_{71}$Mo$_{24}$	12	41 ± 19	24 ± 12	7.2	0.9	25	72
Pt$_5$Ni$_{74}$Mo$_{21}$	8	49 ± 30	17 ± 9	5.6	0.8	88	82

Fig. 3. SEM micrographs of gas diffusion layer (GDL) substrate (a), electrodeposited binary $Pt_{79}Ni_{21}$ (b), $Pt_{67}Ni_{33}$ (c), $Pt_{80}Ni_{20}$ (d), $Pt_{73}Ni_{27}$ (e), and ternary $Pt_{78}Ni_{21}Mo_1$ (f), $Pt_{66}Ni_{32}Mo_2$ (g), $Pt_5Ni_{71}Mo_{24}$ (h), $Pt_5Ni_{74}Mo_{21}$ (i) nanoparticles on the GDL. In the micrographs, the NPs appear brighter than the microporous carbon.
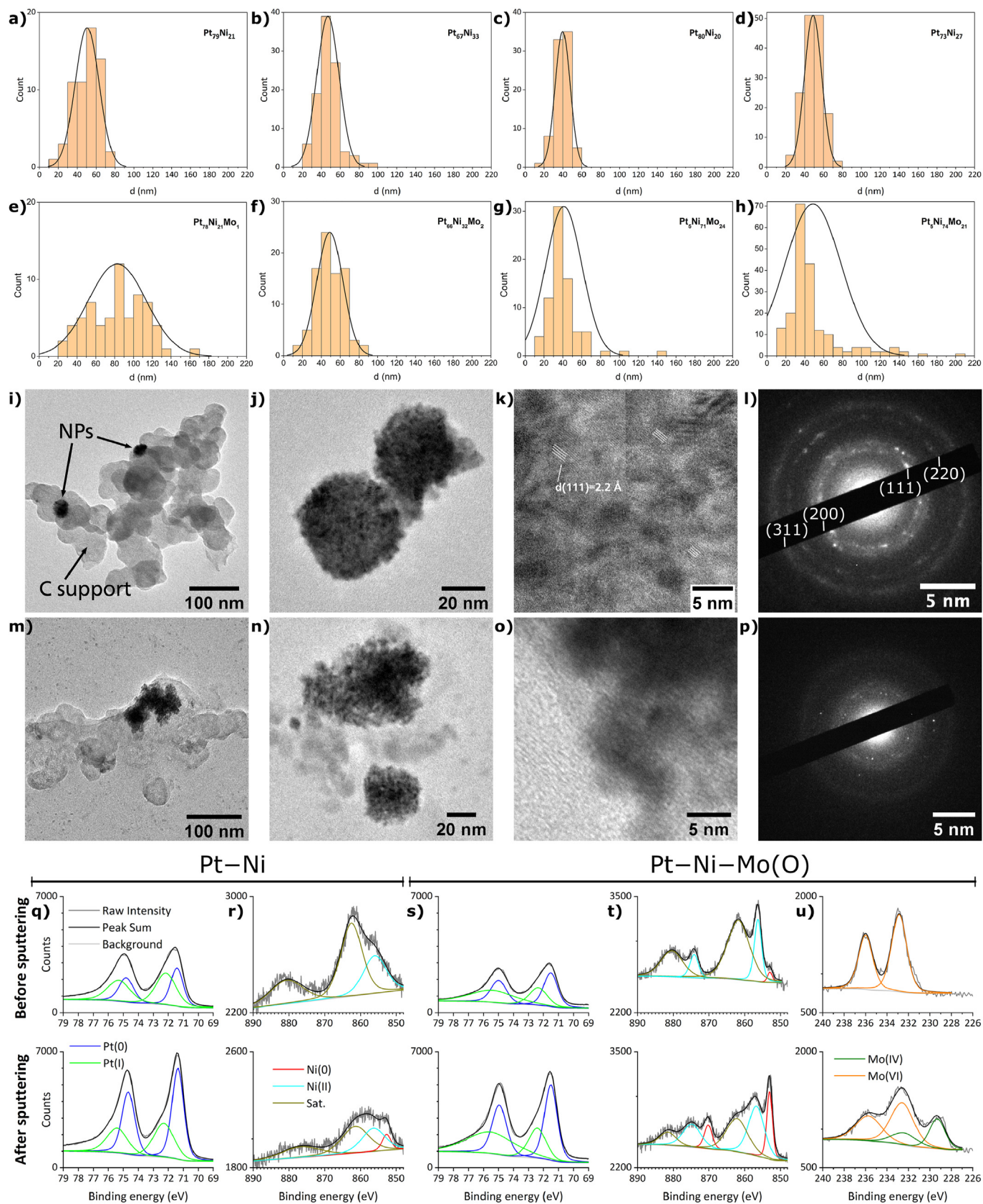
occurrence of oxygen in the Mo-containing NPs originating from incomplete reduction of Mo(VI) precursor was deduced by XPS, as shown later on. The total catalyst loading was less uniform for the Pt–Ni–Mo(O), ranging from 2.5 to 8.1 μg/cm². The current efficiency was also significantly reduced when comparing the ternary Pt–Ni–Mo system to the binary Pt–Ni, with current efficiencies as low as 2–12%.

3.2.2. Microstructural analysis

The GDL substrates show the typical homogeneous microporous layer, consisting of aggregates of globular carbon particles (Fig. 3a). Fluorine emissions in EDX confirmed the presence of PTFE (not shown).
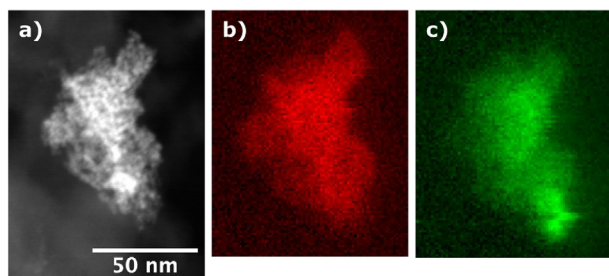
After the pulse electrodeposition, Pt–Ni and Pt–Ni–Mo(O) NPs are homogeneously distributed on the surface and near-surface region of the microporous layer, which appears darker in the SEM images compared with the deposited NPs (Fig. 3). All Pt–Ni NPs show a uniform, spherical shape. The particle size is spread between 20 nm and 80 nm, with an average particle size between 40 nm and 50 nm independent of composition or process parameters (Table 3), and are agglomerated in very few cases (Fig. 3b–e). The Pt–Ni–Mo(O) NPs have the tendency to a spherical structure, although less defined and with higher roughness than the Pt–Ni NPs. While the particle size of $Pt_{78}Ni_{21}Mo_1$ is around 80 nm (Fig. 3f), the other ternary NPs lie between 40 nm and 50 nm. For $Pt_5Ni_{74}Mo_{21}$, a mixture of large (>100 nm) and small (<50 nm) NPs is appreciated (Fig. 3i). This observation is in agreement with the large distribution in particle size determined for this composition, while all other compositions show relatively narrow size distributions (Fig. 4a–h). While commercial Pt/C has significantly smaller
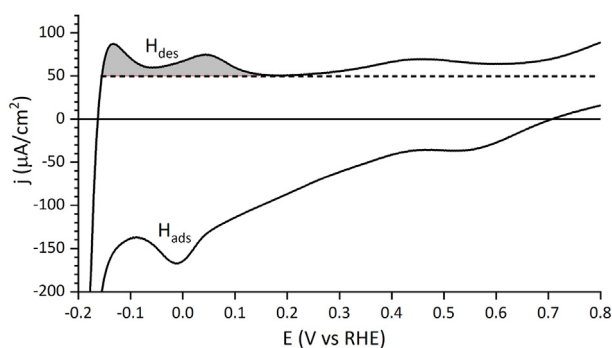
Fig. 4. (a–h) Particle size distribution of Pt$_{79}$Ni$_{21}$ (a), Pt$_{67}$Ni$_{33}$ (b), Pt$_{80}$Ni$_{20}$ (c), Pt$_{73}$Ni$_{27}$ (d), Pt$_{78}$Ni$_{21}$Mo$_1$ (e), Pt$_{66}$Ni$_{32}$Mo$_2$ (f), Pt$_5$Ni$_{71}$Mo$_{24}$ (g), and Pt$_5$Ni$_{74}$Mo$_{21}$ (h) NPs. (i–p) TEM micrographs of C-supported Pt$_{67}$Ni$_{33}$ (top, i–l) and Pt$_{78}$Ni$_{21}$Mo$_1$ (bottom, m–p) NPs (i,j,m,n), in high resolution (k,o), and SAED pattern for a single NP (l,p). (q–u) XPS detail spectra of Pt4f (q) and Ni2p (r) of Pt$_{73}$Ni$_{27}$ NPs and of Pt4f (s), Ni2p (t) and Mo3d (u) of Pt$_5$Ni$_{71}$Mo$_{24}$ NPs before (top) and after sputtering (bottom).

Fig. 5. Dark field TEM image (a) and element distribution of Pt (b) and Ni (c) determined by electron energy loss spectroscopy on a $Pt_5Ni_{74}Mo_{21}$ nanoparticle.

Fig. 6. Representative cyclic voltammetry of gas diffusion layer–supported $Pt_{73}Ni_{27}$ in 0.5 M H_2SO_4 for the determination of electrochemically active surface area. The integrated area of the hydrogen desorption peak is displayed in gray.

particle size, Fouda-Onana et al. electrodeposited Pt particles with a size of 50 nm and found that despite the larger particle size, the utilization rate was high due to all particles having triple phase boundaries (TPBs) [39].

In TEM observations, the Pt–Ni and Pt–Ni–Mo(O) NPs are clearly distinguished from the C support by phase contrast (in bright field TEM, the NPs appear darker than the carbon-based support; Fig. 4i,m). The binary NPs are of well-defined, globular form, whereas the ternary NPs are more irregular (Fig. 4j,n). The high-resolution mode reveals the nanocrystalline structure of Pt–Ni NPs, indicated by diffraction planes with different orientations (Fig. 4k). This nanocrystallinity is also clearly observed in the selected area electron diffraction (SAED) pattern of a single NP with a diameter (ø) <50 nm, where almost any diffraction direction is present, confirmed by the quasi-continuous rings observed in the pattern (Fig. 4l). The corresponding d-spacings match the face-centered cubic (fcc) phase for a Pt–Ni alloy. For $Pt_{67}Ni_{33}$, the average cell parameter determined from SAED was 3.88 Å, which corresponds well with the d(111) spacing of 2.2 Å measured in the high-resolution image.

In contrast to the Pt–Ni NPs, the Pt–Ni–Mo(O) NPs show more diffuse diffraction rings, which are more characteristic of an amorphous material, even when the Mo content is very low (Fig. 4p). Some additional diffraction spots indicate the presence of Mo oxide species such as MoO_3 or other non-stoichiometric oxides [40]. Diffraction planes in high-resolution TEM are only appreciated in extremely few occasions at the NPs' surfaces, showing crystals smaller than 5 nm (Fig. 4o). Other than that, diffraction planes are not observed, leading to the conclusion that most Pt–Ni crystals are too small to diffract and that they are completely mixed in with the molybdenum oxide species in a sort of composite.

From SAED data, the existence of a homogeneous alloy is clear for the Pt–Ni NPs, the ternary Pt–Ni–Mo(O) NPs were analyzed

by EELS to confirm the distribution of Pt, Ni, and Mo. However, even for the NPs with the highest Mo content ($Pt_5Ni_{74}Mo_{21}$), Mo was not detectable by EELS due to the high delay of the Mo signal, and the high amount of carbon causing a large background signal (and resulting in a very low Mo content with respect to carbon). In contrast, Pt and Ni are clearly distributed evenly over the NPs (Fig. 5).

3.2.3. XPS

The Pt4f spectra of the surfaces of the deposited Pt–Ni NPs, exemplary shown for $Pt_{73}Ni_{27}$, show emissions of metallic Pt at 71.4 eV and of Pt(I) at 72.3 eV, which can be assigned to platinum hydroxide [41]. In the Ni2p spectra, no contribution of metallic Ni is observed and most superficial Ni is bound in $Ni(OH)_2$ (Fig. 4q,r).

After Ar ion sputtering, the XPS spectra show a contribution of metallic Ni, as well as a higher fraction of metallic Pt with respect to the hydroxide species. It must be noted that, in contrast to bulk material, the contribution of the NPs' surface cannot be eliminated by sputtering. This means that after sputtering, there is still a significant contribution of the surface state, and the actual bulk state at the NPs' cores is assumed to contain even higher fractions of metallic and less oxidized species than represented in the XPS spectra after Ar ion sputtering.

For the ternary Pt–Ni–Mo(O) NPs, very similar observations are made with respect to the Pt4f and Ni2p emissions (Fig. 4s and t). The Mo3d detail spectra do not show any evidence of metallic Mo at 228.0 eV [41]. The initial surface state shows the occurrence of Mo(VI) exclusively, which points to the presence of MoO_3. After sputtering, the lower oxidation state Mo(IV) is found, which may correspond to MoO_2 (Fig. 4u). Therefore, Mo(VI) was not fully reduced to Mo(0) in spite of the presence of Ni(II) and citrate in the electrolyte. It can be argued that sufficient complexing of molybdate species with citrate, and therefore the full discharge of Mo(VI) to Mo(0), does not occur at the rather low pH of the electrolyte of 2.7. At this pH, the citrate mostly exists in its protonated form, thus hindering complexation of metal ions.

For both binary and ternary NPs, a drastic reduction of O1s emissions (not shown) were observed after sputtering, indicating that the NPs exhibit an oxidized surface and a metallic core. Due to the fact that contributions of the NPs' surfaces are present even after sputtering, O1s emissions are not completely suppressed, nor can it be completely ruled out that there remain low amounts of residual oxygen in the NPs' cores.

Combining all knowledge obtained on the ternary Pt–Ni–Mo system, the following conclusions can be drawn. Taking into account the existence of Pt(0), Ni(0), Mo(IV), and Mo(VI) shown by XPS, the absence of concrete diffraction rings for the Pt–Ni fcc phase in SAED, the very small (<5 nm) crystalline regions in high resolution TEM, and the homogeneous distribution of Pt and Ni throughout the NPs as evidenced by EELS, it is concluded that Pt–Ni crystals and molybdenum oxide species are coexistent and randomly distributed among the NPs. Thus, the Pt–Ni–Mo(O) NPs consist of a heterogeneous compound of Pt–Ni and molybdenum oxide, which due to their nanosized nature and random distribution, appear as a homogeneous compound even on the nanoscale.

3.3. Half-cell electrochemical tests

The GDL substrates exhibit a rather low electric conductivity, leading to a relatively high double-layer capacitance observed in CV. Nevertheless, the hydrogen adsorption (H_{ads}) and desorption peaks (H_{des}) used for the determination of ECSA are well defined, as shown exemplarily for $Pt_{73}Ni_{27}$ (Fig. 6).

The ECSA of both the Pt−Ni and Pt−Ni−Mo(O) is comparable with what is found in literature (Table 3) [2], showing that despite the electrodeposited catalysts having a large particle size, the Pt utilization is high.

The electrodeposited Pt−Ni and Pt−Ni−Mo(O) NPs all show lower reduction potentials at ORR compared with the Pt/C (Fig. 7a). Among them, the Mo-containing NPs are inferior to the binary alloy NPs with comparable Pt/Ni ratio. Interestingly, the best performance among the electrodeposited NPs is observed for $Pt_{67}Ni_{33}$. A diffusion-controlled region is not observed for any of the samples; this is related to the fact that kinetics is limited because the measurements were carried out in stagnant conditions, and also due to the GDL substrates which are not perfect conductors.
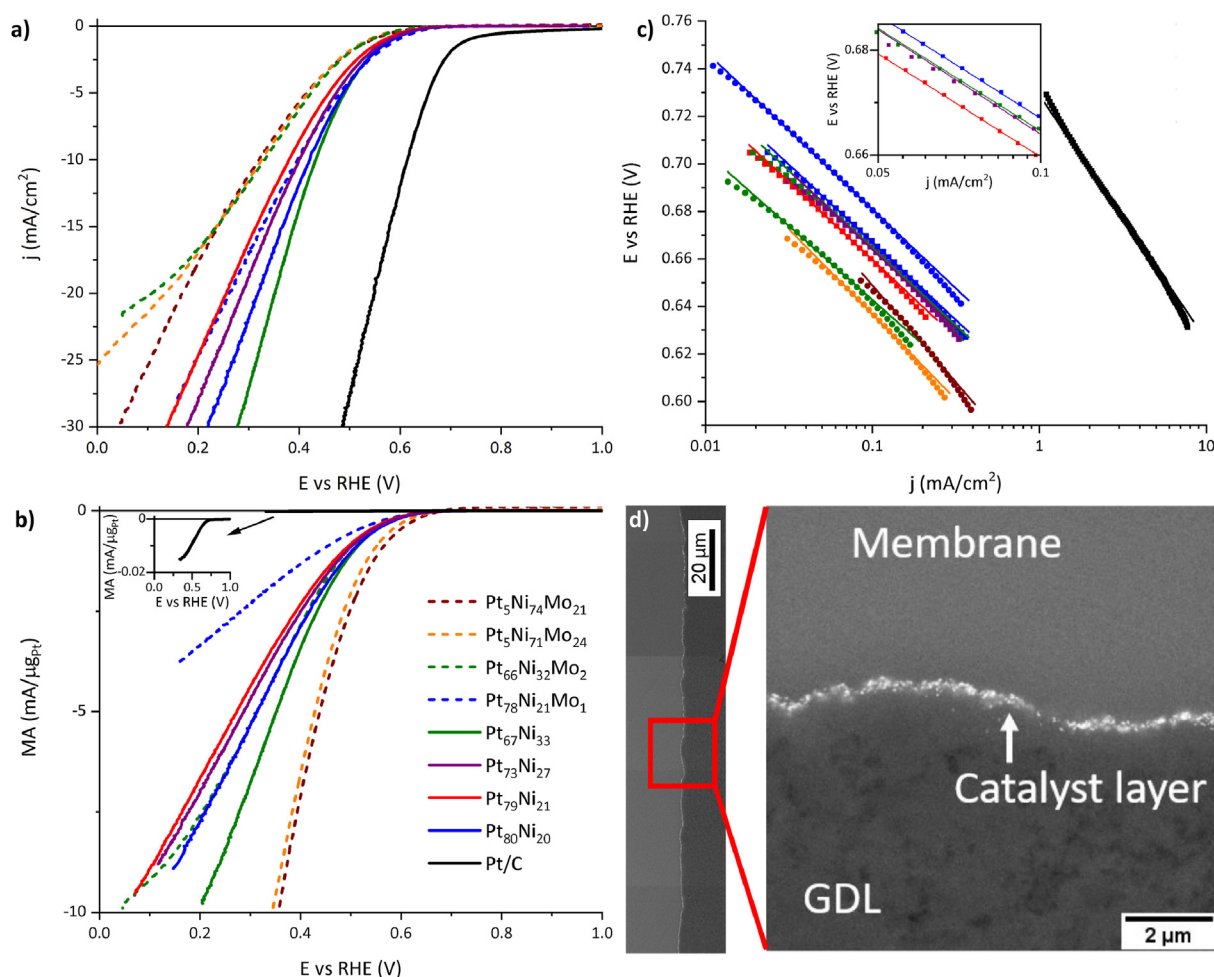
The advantage of electrodeposited Pt−Ni and Pt−Ni−Mo(O) NPs becomes apparent when the Pt mass activity at ORR is considered (Fig. 7b). $Pt_{67}Ni_{33}$ shows the highest Pt mass activity among the binary NPs. In addition, the Ni-rich ternary NPs, which also have significantly higher amounts of Mo, show the highest mass activity with respect to Pt content. This shows that the addition of Mo does not compromise the catalytic activity and may indeed lead to improvement, however, the stability at ORR of these low-Pt content NPs in acidic conditions may be compromised. Liu et al. recently found that a Ni-rich Ni−Pt alloy electrocatalyst can be employed

successfully in PEMFC with only little performance loss over 30 h of constant operation [25]. Among the Pt-rich ternary NPs, $Pt_{66}Ni_{32}Mo_2$ shows the highest Pt mass activity, corresponding to the Ni/Pt ratio of the binary $Pt_{67}Ni_{33}$. Zalitis et al. showed that ultrathin catalyst layers of 200 nm thickness can be employed to overcome limitations by internal resistances such as experienced here with the use of the GDL. In this way, the mass activity can be further increased by one order of magnitude at comparable Pt loading [42].

An increase in total load of electrodeposited NPs on the GDL is expected to increase the half-wave potential at ORR. However, the electrodeposition of higher amounts of catalyst could easily lead to NP growth rather than nucleation of more particles.
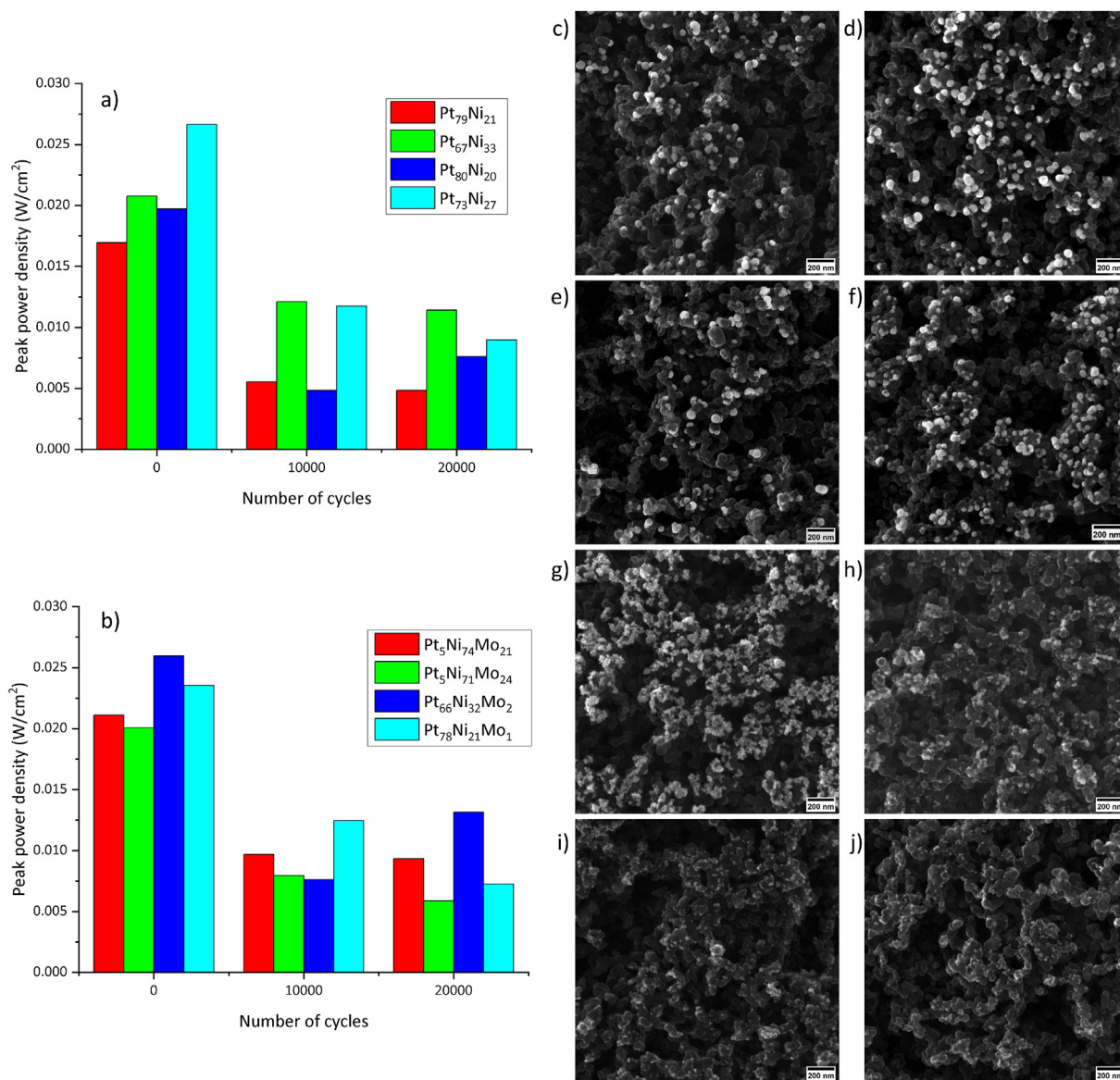
Another way of improving the ORR of the electrodeposited NPs is by addition of an ionomer such as Nafion, which can lead to a significant increase in ECSA and ORR performance by improving the wettability of the GDL [43].

In terms of kinetics, the determined Tafel slopes (b) show a significant improvement with respect to the commercial Pt/C electrode, for which a Tafel slope of 103 mV is obtained. Interestingly, all binary Pt−Ni binary alloy NPs exhibit an almost identical Tafel slope of 65−66 mV (cf. Table 3). The ternary Pt−Ni−Mo(O) NPs show a higher spread in b, where $Pt_{66}Ni_{32}Mo_2$ has the lowest Tafel slope of 62 mV (Fig. 7c). The measured Tafel slopes correspond

Fig. 7. Oxygen reduction reaction of Pt−Ni and Pt−Ni−Mo(O) nanoparticles (NPs) deposited on gas diffusion layer (GDL) in comparison with Pt/C, by geometric current density (a) and by Pt mass activity (b). The inset in (b) shows the mass activity for the Pt/C electrode. Tafel slopes for the GDL-supported Pt−Ni and Pt−Ni−Mo(O) NPs, and for commercial Pt/C (c). The inset in (c) shows a zoom for the closely-placed Pt−Ni NP electrocatalysts. Back-scattered electron micrograph of a cross section of hot-pressed $Pt_{66}Ni_{32}Mo_2$ membrane electrode assembly prior to proton exchange membrane fuel cell testing (d).

Fig. 8. Peak power density of Pt−Ni (a) and Pt−Ni−Mo(O) catalysts (b) after activation, 10 000, and 20 000 accelerated stress test (AST) cycles. SEM micrographs of $Pt_{79}Ni_{21}$ (c), $Pt_{67}Ni_{33}$ (d), $Pt_{80}Ni_{20}$ (e), $Pt_{73}Ni_{27}$ (f), $Pt_{78}Ni_{21}Mo_1$ (g), $Pt_{66}Ni_{32}Mo_2$ (h), $Pt_5Ni_{71}Mo_{24}$ (i), and $Pt_5Ni_{74}Mo_{21}$ (j) nanoparticles on the gas diffusion layer after AST in the proton exchange membrane fuel cell.

well with the one determined by Fortunato et al. on pure Pt NPs synthesized by electrodeposition [44].
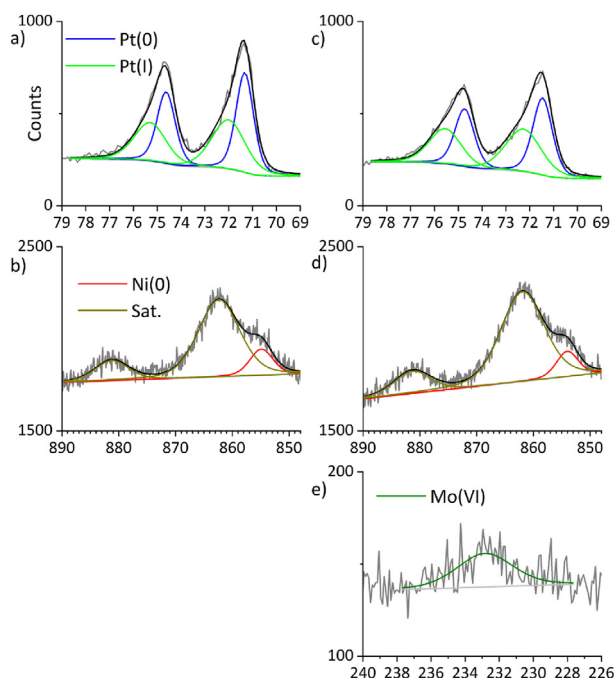
3.4. Proton exchange membrane fuel cell testing

The cross-sectional image of a hot-pressed MEA prior to testing in the fuel cell shows that the catalyst layer (CL) formed by the electrodeposited NPs is homogeneous and well adhered to the membrane, ensuring proton conductivity (Fig. 7d).

The polarization curves show that the low catalyst loading results in low current density (not shown). However, the catalysts activity is similar independent of composition, both initially and after AST. Interestingly, the $Pt_{67}Ni_{33}$ and $Pt_{66}Ni_{32}Mo_2$ again show the highest activity. The major drop in PEMFC performance takes place during the first 10 000 cycles, whereas there is not as significant drop from 10 000 to 20 000 AST cycles (Fig. 8). This is in accordance with literature [2] and can be explained by the

dissolution of unstable catalytic sites, such as surface Ni and Mo in the initial half of the AST, leaving the particles more stable in the second half of the AST. No decrease in activity could be seen for the commercial Pt/C, which after 20 000 AST cycles show a peak power density of 0.377 W/cm^2.

In general, the SEM micrographs of the NPs after AST in the PEMFC show that the particle size is reduced (cf. Table 3), related to a loss of material by dissolution in the acidic environment (Fig. 8). The exception is $Pt_{80}Ni_{20}$, where the particle size is slightly increased (Table 3). This increase in particle size can be explained by Pt dissolution from smaller, less stable particles, and re-deposition onto larger particles. It should be noted that a non-negligible amount of particles remained attached to the membrane rather than the GDL after disassembling the MEA for post-analysis. The Pt−Ni particles have kept their spherical morphology, while the Pt−Ni−Mo(O) NPs have increased roughness after testing. It is also clear that the two Ni-rich samples with very low Pt content

Fig. 9. XPS detail spectra of Pt4f (a) and Ni2p (b) of $Pt_{73}Ni_{27}$ nanoparticles (NPs) and of Pt4f (c), Ni2p (d) and Mo3d (e) of $Pt_5Ni_{71}Mo_{24}$ NPs after proton exchange membrane fuel cell tests.

4. Conclusions

Binary Pt−Ni and ternary Pt−Ni−Mo(O) NPs were successfully synthesized by pulse electrodeposition from aqueous media directly onto the GDL of a PEMFC. The so-prepared carbon-supported catalysts show high specific activities at ORR and the applicability in PEMFC was demonstrated in a single-cell, with $Pt_{67}Ni_{33}$ and $Pt_{66}Ni_{32}Mo_2$ showing the highest activity both in ORR measurements and in the PEMFC.

NP particle sizes range around 50 nm, and Tafel slopes at ORR of around 65 mV are achieved at low catalyst loadings of 4 μg/cm². Most importantly, very high ORR mass activities up to 10 mA/μg$_{Pt}$ are reached at half-cell electrochemical tests in 0.1 M HClO₄, owing to the favorable distribution of electrocatalyst NPs along the catalyst layer as a result of the electrodeposition process. In the MEAs produced for PEMFC testing, almost all NPs are expected to contribute to the ORR reaction due to their direct contact with both carbon support and PEM, resulting in extremely high efficiency with respect to Pt utilization.

For industrial application in PEMFC, the total power output of the fuel cell would need to be increased. To this respect, a higher total amount of catalyst may be needed, achieved by either increasing the Pt load in electrodeposition or by increasing the fuel cell's active area. An increase of loading by electrodeposition is easily achievable. However, by simply increasing the deposition time, additional deposition will occur on already deposited material and lead to particle growth. This would most likely improve half-wave potential and obtainable currents, but adversely affect mass activity. Further optimization is possible by tuning the NP particle size, or by optimizing the electrical properties by the use of thin carbon layers adapted to electrodeposition, to reduce intrinsic resistances.

With respect to the ternary system NPs, an obvious advantage over binary Pt−Ni NPs is not observed. Since Mo was mostly found in an oxidized state and the crystallinity of the ternary NPs as observed by SAED was lower, the question remains open as to whether a true, metallic ternary alloy would yield superior ORR activity.

Overall, the demonstrated electrodeposition process provides a promising alternative to the conventional methods of ORR electrocatalyst synthesis. In addition to the facile synthesis which applies the catalyst NPs directly onto the GDL, the utilization of the metal electrocatalyst can be seen as close to 100%.

CRediT author statement

Konrad Eiler: conceptualization, validation, formal analysis, investigation, data curation, writing—original draft, writing—review & editing, visualization. **Live Mølmen:** conceptualization,

experience the most severe dissolution of catalyst material. However, the PEMFC performance at EoT is similar to the other samples. This may be due to the high surface area endowed by the rough morphology of these NPs.

The XPS spectra obtained from the catalyst layers after PEMFC testing are compromised by the aforementioned loss of material due to particles remaining on the membrane; however, it was generally observed that in comparison with the initial surface state, both Pt(0) and Ni(0) were present in higher fractions with respect to their oxidized forms (Fig. 9). For the Mo-containing catalysts, only Mo(VI) was detected after the PEMFC tests. Contrarily to what might be expected, Ni2p emission levels are close to their initial values (cf. Fig. 4q−u) while Pt emissions are significantly lower.

Although electrodeposition is a very common and widely used synthesis method, its employment in the synthesis of ORR electrocatalysts for PEMFC is rather unexplored. Few studies have investigated this topic in recent years, and the processes need to be further optimized in view of the electrocatalysts' properties and performance, and especially in terms of actual testing in PEMFC (Table 4).

Table 4
Comparison of electrodeposited catalysts for oxygen reduction reaction (ORR) in proton exchange membrane fuel cell (PEMFC) reported in literature.

Material	Particle size nm	Pt loading μg/cm²	ECSA m²/g$_{Pt}$	b mV	PEMFC operation	Reference
Pt−Ni	47	4.0	19	65	Successful	This work
Pt−Ni−Mo(O)	49	2.2	18	62	Successful	This work
Pt−Ni	Thin film	27	27		−	[29]
Pt−Ni−Co	ca. 100	52		153	−	[45]
Pt	ca. 50	6.2	155	63	−	[44]
Pt	89	1.6	46		−	[16]
Pt	3−10	9.5			−	[23]
Pt	ca. 1 000	<100			Successful	[19]
Pt		90	23		Successful	[13]
Pt−Co		300 (Pt + Co)			Successful	[13]
Pt−Co	ca. 1 000	500			In DMFC[a]	[35]
Pt−Co			6.5 mC/cm²		−	[20]

[a] Direct methanol fuel cell.

software, validation, formal analysis, investigation, data curation, writing—original draft, writing—review & editing, visualization. **Lars Fast:** conceptualization, methodology, validation, resources, supervision, project administration. **Peter Leisner:** conceptualization, resources, supervision, project administration, funding acquisition. **Jordi Sort:** conceptualization, resources, writing—review & editing, supervision, funding acquisition. **Eva Pellicer:** conceptualization, validation, resources, writing—review & editing, supervision, project administration, funding acquisition.

Data availability

The raw/processed data required to reproduce these findings cannot be shared at this time due to technical or time limitations. Specific data can be obtained from the corresponding authors on request.

Declaration of competing interest

The authors declare that they have no known competing financial interests or personal relationships that could have appeared to influence the work reported in this paper.

Acknowledgement

References

[1] European Commission, A Hydrogen Strategy for a Climate-Neutral Europe, 2020. COM(2020) 301 final.
[2] L. Mølmen, K. Eiler, L. Fast, P. Leisner, E. Pellicer, Recent advances in catalyst materials for proton exchange membrane fuel cells, APL Mater. 9 (2021), 040702, https://doi.org/10.1063/5.0045801.
[3] L. Mølmen, A. Alexandersson, P. Leisner, Surface technology should improve PEM fuel cell performance, Trans. IMF 97 (2019) 112, https://doi.org/10.1080/00202967.2019.1596573.
[4] J.K. Nørskov, J. Rossmeisl, A. Logadottir, L. Lindqvist, J.R. Kitchin, T. Bligaard, H. Jónsson, Origin of the overpotential for oxygen reduction at a fuel-cell cathode, J. Phys. Chem. B 108 (2004) 17886, https://doi.org/10.1021/jp047349j.
[5] K. Kodama, T. Nagai, A. Kuwaki, R. Jinnouchi, Y. Morimoto, Challenges in applying highly active Pt-based nanostructured catalysts for oxygen reduction reactions to fuel cell vehicles, Nat. Nanotechnol. 16 (2021) 140, https://doi.org/10.1038/s41565-020-00824-w.
[6] Y. Yang, C. Tan, Y. Yang, L. Zhang, B.-W. Zhang, K.—H. Wu, S. Zhao, Pt₃Co@Pt core@shell nanoparticles as efficient oxygen reduction electrocatalysts in direct methanol fuel cell, ChemCatChem 13 (2021) 1587, https://doi.org/10.1002/cctc.202001868.
[7] Z. Wang, X. Yao, Y. Kang, D. Xia, L. Gan, Rational development of structurally ordered platinum ternary intermetallic electrocatalysts for oxygen reduction reaction, Catalysts 9 (2019) 569, https://doi.org/10.3390/catal9070569.
[8] L. Huang, M. Wei, N. Hu, P. Tsiakaras, P. Kang Shen, Molybdenum-modified and vertex-reinforced quaternary hexapod nano-skeletons as efficient electrocatalysts for methanol oxidation and oxygen reduction reaction, Appl. Catal., B 258 (2019) 117974, https://doi.org/10.1016/j.apcatb.2019.117974.
[9] S. Zhao, Y. Yang, Z. Tang, Insight into structural evolution, active sites, and stability of heterogeneous electrocatalysts, Angew. Chem. Int. Ed. 61 (2022), e202110186, https://doi.org/10.1002/anie.202110186.
[10] X. Wang, Y. Li, C. Yang, J. Lu, L. Cao, H.—P. Liang, Surfactant-assisted implantation strategy for facile construction of Pt-based hybrid electrocatalyst to accelerate oxygen reduction reaction, Mater. Today Energy 24 (2022) 100919, https://doi.org/10.1016/j.mtener.2021.100919.
[11] P. Yin, B. You, Atom migration-trapping toward single-atom catalysts for energy electrocatalysis, Mater. Today Energy 19 (2021) 100586, https://doi.org/10.1016/j.mtener.2020.100586.
[12] J. Hou, M. Yang, C. Ke, G. Wei, C. Priest, Z. Qiao, G. Wu, J. Zhang, Platinum-group-metal catalysts for proton exchange membrane fuel cells: from catalyst design to electrode structure optimization, Energy Chem. 2 (2020) 100023, https://doi.org/10.1016/j.enchem.2019.100023.
[13] A. Egetenmeyer, I. Radev, D. Durneata, M. Baumgärtner, V. Peinecke, H. Natter, R. Hempelmann, Pulse electrodeposited cathode catalyst layers for PEM fuel cells, Int. J. Hydrog. Energy 42 (2017) 13649, https://doi.org/10.1016/j.ijhydene.2017.01.212.
[14] J. Ustarroz, T. Altantzis, J.A. Hammons, A. Hubin, S. Bals, H. Terryn, The role of nanocluster aggregation, coalescence, and recrystallization in the electrochemical deposition of platinum nanostructures, Chem. Mater. 26 (2014) 2396, https://doi.org/10.1021/cm403178b.
[15] J. Ustarroz, B. Geboes, H. Vanrompay, K. Sentosun, S. Bals, T. Breugelmans, A. Hubin, Electrodeposition of highly porous Pt nanoparticles studied by quantitative 3D electron tomography: influence of growth mechanisms and potential cycling on the active surface area, ACS Appl. Mater. Interfaces 9 (2017) 16168, https://doi.org/10.1021/acsami.7b01619.
[16] B. Geboes, J. Ustarroz, K. Sentosun, H. Vanrompay, A. Hubin, S. Bals, T. Breugelmans, Electrochemical behavior of electrodeposited nanoporous Pt catalysts for the oxygen reduction reaction, ACS Catal. 6 (2016) 5856, https://doi.org/10.1021/acscatal.6b00668.
[17] J.H. Park, H.S. Ahn, Electrochemical synthesis of multimetallic nanoparticles and their application in alkaline oxygen reduction catalysis, Appl. Surf. Sci. 504 (2020) 144517, https://doi.org/10.1016/j.apsusc.2019.144517.
[18] F. Alcaide, G. Álvarez, P.L. Cabot, R.V. Genova-Koleva, H.—J. Grande, M.V. Martínez-Huerta, O. Miguel, Supporting PtRh alloy nanoparticle catalysts by electrodeposition on carbon paper for the ethanol electrooxidation in acidic medium, J. Electroanal. Chem. 861 (2020) 113960, https://doi.org/10.1016/j.jelechem.2020.113960.
[19] C. Huang, C.B. Odetola, M. Rodgers, Nanoparticle seeded pulse electrodeposition for preparing high performance Pt/C electrocatalysts, Appl. Catal. A 499 (2015) 55, https://doi.org/10.1016/j.apcata.2015.03.043.
[20] J. Sriwannaboot, A. Kannan, N. Tantavichet, Pulse-reverse electrodeposition of Pt—Co bimetallic catalysts for oxygen reduction reaction in acidic medium, Int. J. Hydrog. Energy 45 (2020) 7025, https://doi.org/10.1016/j.ijhydene.2019.12.191.
[21] A. Egetenmeyer, M. Baumgärtner, T. Linckh, D. Durneata, H. Natter, R. Hempelmann, I. Radev, V. Peinecke, Pulse electrodeposition of catalyst nanoparticles for application in PEM fuel cells, Trans. IMF 95 (2017) 9, https://doi.org/10.1080/00202967.2017.1253661.
[22] D. Santiago, G.G. Rodríguez-Calero, H. Rivera, D.A. Tryk, M.A. Scibioh, C.R. Cabrera, Platinum electrodeposition at high surface area carbon Vulcan-XC-72R material using a rotating disk-slurry electrode technique, J. Electrochem. Soc. 157 (2010) F189, https://doi.org/10.1149/1.3489948.
[23] D. Wang, G. Hu, P. Yang, X. Pan, H. Xu, L. Liu, J. Zhang, M. An, Using DMH as a complexing agent for pulse electrodeposition of platinum nanoparticles towards oxygen reduction reaction, Ionics 26 (2020) 3473, https://doi.org/10.1007/s11581-019-03427-1.
[24] C. Qiu, S. Wang, R. Gao, J. Qin, W. Li, X. Wang, Z. Zhai, D. Tian, Y. Song, Low-temperature synthesis of PdO-CeO₂/C toward efficient oxygen reduction reaction, Mater, Today Energy 18 (2020) 100557, https://doi.org/10.1016/j.mtener.2020.100557.
[25] X. Liu, X. Wan, X. Tan, H. Yang, Y. Yang, J. Shui, X. Wang, Nanoscale Pt₅Ni₃₆ design and synthesis for efficient oxygen reduction reaction in proton exchange membrane fuel cells, J. Mater. Chem. 9 (2021) 21051, https://doi.org/10.1039/d1ta05189j.
[26] E. Antolini, The oxygen reduction on Pt-Ni and Pt-Ni-M catalysts for low-temperature acidic fuel cells: a review, Int. J. Energy Res. 42 (2018) 3747, https://doi.org/10.1002/er.4134.
[27] X. Tian, X. Zhao, Y.—Q. Su, L. Wang, H. Wang, D. Dang, B. Chi, H. Liu, E.J.M. Hensen, X.W. Lou, B.Y. Xia, Engineering bunched Pt-Ni alloy nanocages for efficient oxygen reduction in practical fuel cells, Science 366 (2019) 850, https://doi.org/10.1126/science.aaw7493.
[28] K. Eiler, S. Suriñach, J. Sort, E. Pellicer, Mesoporous Ni-rich Ni-Pt thin films: electrodeposition, characterization and performance toward hydrogen evolution reaction in acidic media, Appl. Catal., B 265 (2020) 118597, https://doi.org/10.1016/j.apcatb.2020.118597.
[29] Y. Liu, C.M. Hangarter, U. Bertocci, T.P. Moffat, Oxygen reduction reaction on electrodeposited Pt₁₀₀₋ₓNiₓ: influence of alloy composition and dealloying, J. Phys. Chem. C 116 (2012) 7848, https://doi.org/10.1021/jp300672h.
[30] X. Huang, Z. Zhao, L. Cao, Y. Chen, E. Zhu, Z. Lin, M. Li, A. Yan, A. Zettl, Y.M. Wang, X. Duan, T. Mueller, Y. Huang, High-performance transition metal-doped Pt₃Ni octahedra for oxygen reduction reaction, Science 348 (2015) 1230, https://doi.org/10.1126/science.aaa8765.
[31] E. Chassaing, N. Portail, A.—F. Levy, G. Wang, Characterisation of electrodeposited nanocrystalline Ni—Mo alloys, J. Appl. Electrochem. 34 (2004) 1085, https://doi.org/10.1007/s10800-004-2460-z.
[32] E. Gómez, E. Pellicer, E. Vallés, Intermediate molybdenum oxides involved in binary and ternary induced electrodeposition, J. Electroanal. Chem. 580 (2005) 238, https://doi.org/10.1016/j.jelechem.2005.03.031.
[33] Z. Liu, J.E. Hu, Q. Wang, K. Gaskell, A.I. Frenkel, G.S. Jackson, B. Eichhorn, PtMo alloy and MoOₓ@Pt core-shell nanoparticles as highly CO-tolerant electrocatalysts, J. Am. Chem. Soc. 131 (2009) 6924, https://doi.org/10.1021/ja901303d.

[34] C. Wang, D. Wang, S. Liu, P. Jiang, Z. Lin, P. Xu, K. Yang, J. Lu, H. Tong, L. Hu, W. Zhang, Q. Chena, Engineering the coordination environment enables molybdenum single-atom catalyst for efficient oxygen reduction reaction, J. Catal. 389 (2020) 150, https://doi.org/10.1016/j.jcat.2020.05.034.

[35] O. Sorsa, H. Romar, U. Lassi, T. Kallio, Co-electrodeposited mesoporous PtM (M=Co, Ni, Cu) as an active catalyst for oxygen reduction reaction in a polymer electrolyte membrane fuel cell, Electrochim. Acta 230 (2017) 49, https://doi.org/10.1016/j.electacta.2017.01.158.

[36] S.A. Lee, J.W. Yang, S. Choi, H.W. Jang, Nanoscale electrodeposition: Dimension control and 3D conformality, Exploration 1 (2021) 20210012, https://doi.org/10.1002/exp.20210012.

[37] E.J. Podlaha, D. Landolt, Induced codeposition: I. An experimental investigation of Ni-Mo alloys, J. Electrochem. Soc. 143 (1996) 885, https://doi.org/10.1149/1.1836553.

[38] C. Wei, R.R. Rao, J. Peng, B. Huang, I.E.L. Stephens, M. Risch, Z.J. Xu, Y. Shao-Horn, Recommendation practices and benchmark activity for hydrogen and oxygen electrocatalysis in water splitting and fuel cells, Adv. Mater. 31 (2019) 1806296, https://doi.org/10.1002/adma.201806296.

[39] F. Fouda-Onana, N. Guillet, A.M. Almayouf, Modified pulse electrodeposition of Pt nanocatalyst as high-performance electrode for PEMFC, J. Power Sources 271 (2014) 401, https://doi.org/10.1016/j.jpowsour.2014.08.031.

[40] A. Quintana, A. Varea, M. Guerrero, S. Suriñach, M.D. Baró, J. Sort, E. Pellicer, Structurally and mechanically tunable molybdenum oxide films and patterned submicrometer structures by electrodeposition, Electrochim. Acta 173 (2015) 705, https://doi.org/10.1016/j.electacta.2015.05.112.

[41] J.F. Moulder, W.F. Stickle, P.E. Sobol, K.D. Bomben, Handbook of X-Ray Photoelectron Spectroscopy, Physical Electronics, Inc., MI, 1995.

[42] C.M. Zalitis, D. Kramer, A.R. Kucernak, Electrocatalytic performance of fuel cell reactions at low catalyst loading and high mass transport, Phys. Chem. Chem. Phys. 15 (2013) 4329, https://doi.org/10.1039/c3cp44431g.

[43] P. Mardle, G. Thirunavukkarasu, S. Guan, Y.—L. Chiu, S. Du, Comparative study of PtNi nanowire array electrodes toward oxygen reduction reaction by half-cell measurement and PEMFC test, ACS Appl. Mater. Interfaces 12 (2020) 42832, https://doi.org/10.1021/acsami.0c11531.

[44] G.V. Fortunato, F. de Lima, G. Maia, Oxygen-reduction reaction strongly electrocatalyzed by Pt electrodeposited onto graphene or graphene nanoribbons, J. Power Sources 302 (2016) 247, https://doi.org/10.1016/j.jpowsour.2015.10.069.

[45] M. Li, Y. Lei, N. Sheng, T. Ohtsuka, Preparation of low-platinum-content platinum-nickel, platinum-cobalt binary alloy and platinum-nickel-cobalt ternary alloy catalysts for oxygen reduction reaction in polymer electrolyte fuel cells, J. Power Sources 294 (2015) 420, https://doi.org/10.1016/j.jpowsour.2015.06.084.

Konrad Eiler obtained his PhD in Materials Science from the Universitat Autònoma de Barcelona in 2021, focusing on the electrodeposition of nickel-based materials for electrocatalysis, and included long-term stays at RISE Research Institutes of Sweden and AGH University of Science and Technology, Kraków. Previously, he completed his B.Sc. in Materials Science at TU Darmstadt and his M.Sc. in the same field at TU Berlin in 2014, including an internship at Volkswagen's R&D department in Wolfsburg. Prior to his PhD, Konrad Eiler has been working at the European Organization for Nuclear Research (CERN), Geneva, for over 2 years.

Live Mølmen is a PhD student at Jönköping University in the Department of Materials and Manufacturing, with employment at RISE Research Institutes of Sweden AB. Her PhD focuses on materials reliability in PEM fuel cells and has included secondments to both the University of Udine, Italy, and Universitat Autònoma de Barcelona. Prior to her PhD studies, she obtained an MSc in Materials Technology from the Norwegian University of Science and Technology (NTNU).

Lars Fast, senior researcher at RISE AB since 2001. Received his PhD from Uppsala University in the field of computational material science (1998). He worked as a post-doc in Würzburg, Germany, between 1998 and 2001, in developing and implementing density functional theory for superconductors. At RISE, he has worked mainly with batteries, fuel cells and electrical contacts, including the environmental durability questions and lifetime assessments.

Prof. **Peter Leisner**, head of Materials and Manufacturing Department at School of Engineering, Jönköping University. MSc in electrochemistry (1989) and PhD in pulse plating (1992), Technical University of Denmark. 30 years of experience in applied research in micro-technology, surface technology, and reliability.

Prof. **Jordi Sort** received his PhD Degree in Materials Science from Universitat Autònoma de Barcelona (UAB) in 2002. He worked for 2 years as Postdoctoral Researcher at the SPINTEC Laboratory (Grenoble) and subsequently stayed 6 months at Argonne National Laboratory (USA). He also performed long-term secondments at the Grenoble High Magnetic Fields Laboratory and at Los Alamos National Laboratory. At present, Prof. Sort leads the "Group of Smart Nanoengineered Materials, Nanomechanics and Nanomagnetism (Gnm3)" at UAB, which focuses its research activities on the synthesis of a wide variety of functional materials and the study of their structural, mechanical, magnetic, and thermal properties.

Eva Pellicer is currently an associate professor at Universitat Autònoma de Barcelona (UAB), Spain. She received her BSc in Chemistry in 2000 and the PhD in Materials Technology in 2005, both from Universitat de Barcelona (UB). So far, Dr. Pellicer has published more than 200 papers in journals like Advanced Functional Materials, Applied Catalysis B: Environmental, ACS Nano, etc. Her current research interests are the electrodeposition and characterization of nanostructured and porous alloys for a variety of applications, ranging from electrocatalysis to magneto-electric applications.